Supplementary material: Twisted $[C_2O_5]^{2-}$-groups in $Ba[C_2O_5]$ pyrocarbonate

Dominik Spahr[*,a], Lkhamsuren Bayarjargal[a], Eiken Haussühl[a], Rita Luchitskaia[a], Alexandra Friedrich[b],
Victor Milman[c], Timofey Fedotenko[d], Björn Winkler[a]

[a]*Goethe University Frankfurt, Institute of Geosciences, Altenhöferallee 1, 60438 Frankfurt, Germany*
[b]*University of Würzburg, Institute of Inorganic Chemistry, Am Hubland, 97074 Würzburg, Germany*
[c]*Dassault Systèmes BIOVIA, 334 Cambridge Science Park, Cambridge CB4 0WN, United Kingdom*
[d]*DESY, Notkestrasse 85, 22607 Hamburg, Germany*

1. Methods

1.1. Sample material

We used hydrothermal synthesis to obtain $BaCO_3$ single crystals, derived from an approach for other carbonates.[1] The crystals were grown using barium chloride dihydrate ($BaCl_2 \cdot 2H_2O$) and ammonium bicarbonate (NH_4HCO_3) as starting materials according to the reaction:

$$BaCl_2 \cdot 2H_2O + 2NH_4HCO_3 \rightarrow$$
$$BaCO_3 \downarrow + 2NH_4Cl + CO_2 \uparrow + 3H_2O \quad (1)$$
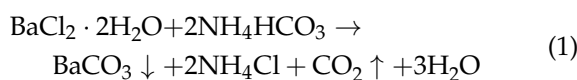
First, 1.5 mmol of analytical grade $BaCl_2 \cdot 2H_2O$ (99.99% purity, Merck, Darmstadt, Germany) was dissolved in 12.5 ml bidistilled water under magnetic stirring at ambient temperature. In addition, 1 mmol of ammonium bicarbonate, NH_4HCO_3 (99.99% purity, Merck, Darmstadt, Germany) was dissolved separately in 25 ml bidistilled water. Afterwards, the resulting solutions were mixed under magnetic stirring at room temperature and the resulting suspension transferred into a 60 ml Teflon cup. The Teflon cup was filled up to 50% of its volume. It was placed in a stainless steel autoclave and heated up to 503(1) K in two hours. The temperature was kept for 24 h. Afterwards, the oven was cooled down in two steps: First from 503(1) K to 453(1) K in 48 h and secondly from 453(1) K to 300(1) K in 24 h. The precipitate was obtained by vacuum filtration, washed with distilled water, and dried in an oven at 333(1) K. We obtained colorless crystals with different crystal habits up to a size of 200 µm.

The CO_2 gas for the gas-jet was used as purchased (Nippon gases, purity ≥ 99.995%).

1.2. High-pressure experiments

The high-pressure experiments were carried out using Boehler-Almax type diamond anvil cells (DACs) with 350 µm culet size and diamonds with 70° opening angle.[2] We used Re-gaskets which were pre-indented to a thickness of ≈ 45 µm. Gasket-holes with 140 µm diameter were drilled by a custom-built laser setup. A $BaCO_3$ crystal with dimensions of ≈ 80 × 40 × 30 µm³ and a ruby chip for pressure determination were placed in the gasket hole. In addition, a piece of pure Re-metal with a diameter of ≈ 10 µm was placed in the gasket hole for the alignment of the X-ray beam. The pressure was determined by measuring the shift of the ruby fluorescence

and we assume an error of 6% due to non-hydrostatic conditions.[3]

CO_2 dry-ice was directly condensed into the gasket hole using a custom-built cryogenic loading system (see Spahr et al.[4]) derived from an earlier concept.[5] The DAC was opened and placed on a liquid nitrogen cooled Cu-holder. It was cooled down to ≈ 100 K and Ar (10 l min^{-1}) was used as a purge-gas to avoid the precipitation of H_2O ice. We used a small nozzle to align a CO_2 gas jet with 5 l min^{-1} directly on the gap between upper diamond and the gasket. The precipitation of the CO_2 in the gasket hole was monitored by an optical microscope and a camera. After a sufficient amount of CO_2 was gathered in the gasket hole, the DAC was tightly closed.

1.3. Raman spectroscopy and laser heating

High-pressure Raman spectroscopy and the double-sided laser-heating in DACs were performed using a custom-built set-up.[6] Raman spectroscopy was performed with an Oxxius LCX-532S Nd:YAG laser ($\lambda = 532.14$ nm) in combination with a Princeton Instruments ACTON SpectraPro (SP-2356) spectrograph equipped with a Pixis 256E CCD camera. Applying a laser power of 250 mW on the sample, the spot size of the Raman laser was ≈ 6 µm. Raman maps were measured on a grid with a step-size of 6 µm and the background was corrected using the software package Fityk.[7]

Double-sided laser-heating was performed using a Coherent Diamond K-250 pulsed CO_2 laser ($\lambda = 10600$ nm). The laser power was adjusted to achieve a coupling of the laser to the sample from both sides (1–3 W) and the focusing on the sample results in a heating area of ≈ 30 × 30 µm². The highest temperature achieved during the laser heating in the different experiments ranged from $T_{max} \approx 1000(200)$ K to $T_{max} \approx 3500(400)$ K. The temperatures were determined by the two-color pyrometer method, employing Planck and Wien fits.[8] The heating time was relatively long (≈ 30 − 90 min). It is well established that laser-heating in DACs always suffers from large temperature gradients and the actual temperature is strongly dependent on the coupling of the laser with the sample, especially at lower temperatures. We estimate an uncertainty of at least ±10% of the nominal temperature in the laser-heated region depending on the focus of the laser beam, based on typical 2D temperature-gradient determination experiments performed in DACs.[9]

1.4. Single crystal synchrotron X-ray diffraction

Single crystal synchrotron X-ray diffraction was carried out at PETRA III (DESY) in Hamburg, Germany, at the extreme conditions beamline P02.2.[10] The beam size on the sample was 1.9 (H) $\times$ 1.9 (V) μm^2 (FWHM), focused by Kirkpatrick Baez mirrors. The diffraction data were collected using a Perkin Elmer XRD1621 detector, a wavelength of 0.2901 Å (42.7 keV) and a detector to sample distance of 396 mm, calibrated from the powder diffraction of a CeO_2 standard and using the software DIOPTAS.[11] We rotated the DAC by $\pm 35°$ around the axes perpendicular to the beam while collecting frames in $0.2°$ steps with 0.5 s acquisition time per frame. The diffractometer/detector geometry was calibrated using diffraction data collected from a single crystal of enstatite ($MgSiO_3$) in a DAC. Before the single crystal data collection, the synchrotron X-ray beam was adjusted on the small Re-piece to ensure a very good positioning and focusing of the beam. Afterwards, the beam was moved to the area where the sample was identified by Raman spectroscopy. After the data collection, the reflections were indexed and integrated employing CrysAlis[PRO] (version 41.122a).[12] The structure solution and refinement were performed using the software package JANA2006 employing SHELXT for the crystal structure determination.[13,14]

1.5. Density functional theory-based calculations

First-principles calculations were carried out within the framework of density functional theory (DFT), employing the Perdew-Burke-Ernzerhof (PBE) exchange-correlation functional and the plane wave/pseudopotential approach implemented in the CASTEP simulation package.[15–17] "On the fly" norm-conserving or ultrasoft pseudopotentials generated using the descriptors in the CASTEP data base were employed in conjunction with plane waves up to a kinetic energy cutoff of 1020 eV or 630 eV, for norm-conserving and ultrasoft pseudopotentials, respectively. The accuracy of the pseudopotentials is well established.[18] A Monkhorst-Pack grid was used for Brillouin zone integrations.[19] We used a distance between grid points of <0.023 Å^{-1}. Convergence criteria for geometry optimization included an energy change of $<5 \times 10^{-6}$ eV atom^{-1} between steps, a maximal force of <0.008 eV Å^{-1} and a maximal component of the stress tensor <0.02 GPa. Phonon frequencies were obtained from density functional perturbation theory (DFPT) calculations.[20,21] Raman intensities were computed using DFPT with the "$2n + 1$" theorem approach.[22]

We used the "virtual crystal approximation" (VCA) to model the Ba-disorder employing ultrasoft pseudopotentials.[23] The VCA neglects local relaxations but allows an efficient calculation of structural parameters.

2. Results

2.1. Raman spectroscopy

We used Raman spectroscopy at ambient conditions to confirm that the hydrothermally synthesized $Ba[CO_3]$ crystals were single phase without impurities. The experimental Raman spectrum is accurately reproduced by the theoretical Raman spectrum obtained from DFT calculations for $Ba[CO_3]$-I with aragonite structure-type and *Pmcn* space group symmetry (Fig. S 1 a). No unexpected Raman modes can be observed in the experimental data.
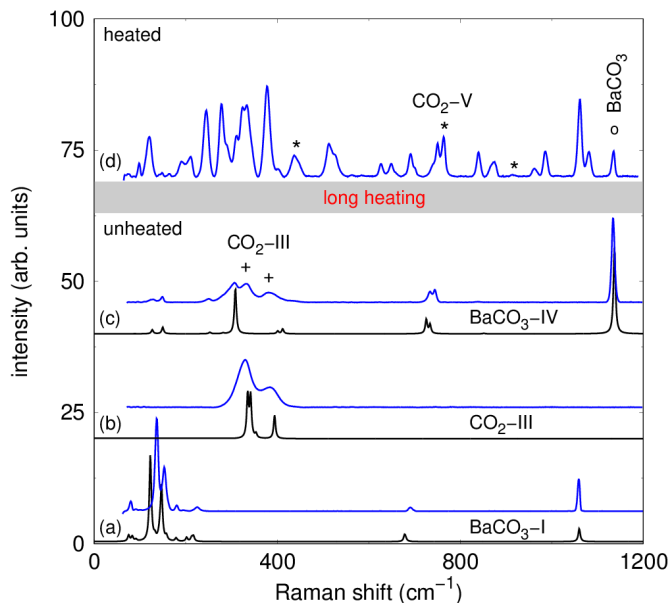

Figure S 1: (a) Experimental Raman spectra for $Ba[CO_3]$-I (blue) compared to DFT-based calculations (black) in aragonite structure-type (*Pmcn*) at 0 GPa. (b) Raman spectra for CO_2-III at 30(2) GPa. (c) Raman spectra for $Ba[CO_3]$-IV (post-aragonite structure-type, *Pmmn*) with peaks of CO_2-III (+) at 30(2) GPa. (d) Raman spectrum of $Ba[C_2O_5]$ after laser heating the $Ba[CO_3]$ + CO_2 mixture at 30(2) GPa to 1500(200) K. Peaks of $Ba[CO_3]$-IV are marked by a circle (○) and of CO_2-V by an asterisk (∗), respectively. The shifts of the calculated Raman spectra were rescaled by 3%.

After cryogenic CO_2 loading and compression to the target pressure of 30 GPa, the edge of the $Ba[CO_3]$ crystal was heated to 1500(200) K. In the unheated areas or the regions which had only been exposed to slightly increased temperatures, CO_2-III and $Ba[CO_3]$-IV are present in the gasket hole of the DAC. The experimental Raman spectra of CO_2-III and $Ba[CO_3]$-IV are in very good agreement with the Raman spectra from the DFT-based calculations at 30 GPa (Fig. S 1 b, c). In contrast, in the directly laser-heated area on the edge of the $Ba[CO_3]$ crystal several new Raman modes can be observed. Figure S 1d shows the Raman spectrum of $Ba[C_2O_5]$ with minor peaks of CO_2 and $Ba[CO_3]$ after the long heating procedure. In addition to CO_2-V, it is possible that metastable CO_2-IV is also present in the Raman spectrum at lower wavenumbers.[24,25] Unfortunately, no theoretical Raman spectrum for $Ba[C_2O_5]$ could be calculated as the computational effort is too high for a structure with a large unit cell and a positional Ba-disorder.

In addition, we measured Raman spectroscopy during decompression of the DAC (Fig. S 2). We found that the characteristic Raman modes of the new $Ba[C_2O_5]$ phase can be observed at least down to 5(1) GPa without significant changes, other than a slight shift of the peak positions to lower wavenumbers. Hence, we assume that $Ba[C_2O_5]$ is not undergoing a phase transition in the examined pressure range (5–30 GPa).

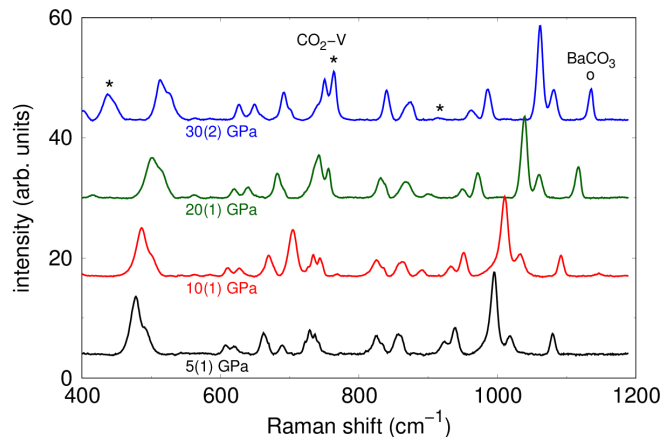**Figure S 2:** Experimental Raman spectra of $Ba[C_2O_5]$ measured during decompression at ambient temperature from 30(2) GPa to 5(1) GPa after the reaction of the $Ba[CO_3]$ + CO_2 mixture at 30(2) GPa and 1500(200) K. Peaks of $Ba[CO_3]$-IV are marked by a circle (○) and of CO_2-V by an asterisk (∗), respectively.

2.2. Single crystal synchrotron X-ray diffraction at 30 GPa

After the identification of a new phase by Raman spectroscopy, the subsequent synchrotron X-ray diffraction was performed in the region where mainly Raman modes of this new phase have been observed in the DACs. The crystal structure of $Ba[C_2O_5]$ was obtained by single crystal X-ray diffraction. Our experimental diffraction data show a very high quality even though they were measured in a DAC at 30(2) GPa and the measured crystal was part of a multi-grain reaction product. Fig. S 3 a shows an *unwarped* image of the raw-experimental data after processing of the (*h0l*) area in CrysAlis. The reflections scatter strongly up to a high resolution in reciprocal space (≤ 0.6 Å^{-1}) and several reflections can be identified at high angles. Except for the very strong reflections of the diamonds, only some weaker reflections of other phases are present apart from the expected reflection positions of $Ba[C_2O_5]$ in the (*h0l*) area. Projections of the reciprocal space show the distribution of reflections and the effect of the shading of diffracted beams due to the DAC in Fig. S 3 b after data reduction. Nevertheless, the coverage of the reciprocal space is satisfactory for DAC experiments and the amount of obtained reflections is very high due to the high X-ray energy, see Table S 1.

First, the crystal structure was solved in the hexagonal space group $P6/m$ (No. 175) with $Z = 12$. In a second step, the experimental data were processed in the triclinic space group $P\bar{1}$ (No. 2) with $Z = 12$ and we observed a slight deviation from the ideal hexagonal angles. After the refinement of both structures, there was no significant difference between both models and both *R*-values

were very low ($R_{P\bar{1}} = 3.3\%$ and $R_{P6/m} = 3.4\%$). This is supported by the *PLATON*/checkCIF program, which suggests $P6/m$ as a new space group with a 100% fit of 6-fold axis by testing the triclinic structural model.[26] Table S 1 lists the crystallographic parameters of Ba[C_2O_5] valid for 30(2) GPa in space group $P6/m$ in comparison to DFT calculations using VCA. The unit cell parameters of the experimental and theoretical structural model match within the expected errors.

Figure S 3: (a) *Unwarped* image of the raw-experimental data after data reduction. The (*h0l*) area is shown. Other reflections are due to other phases present in the sample chamber. (b) Schematic depiction of the reflections in reciprocal space using the Ewald-Explorer in CrysAlis after data reduction and later used for the refinement. Projections of the reciprocal space are shown along b^* (top) and c^* (bottom).

The displacement parameters of the barium, carbon and oxygen atoms were refined anisotropically without any constraints or restraints. The reflection to parameter ratio of 15:1 allows a reliable structure solution and refinement.

Table S 1: Structural parameters of disordered Ba[C_2O_5] at 30(2) GPa from single crystal structure solution (ambient temperature) in hexagonal space group $P6/m$ in comparison to theoretical data derived from DFT calculations (athermal limit) using VCA .
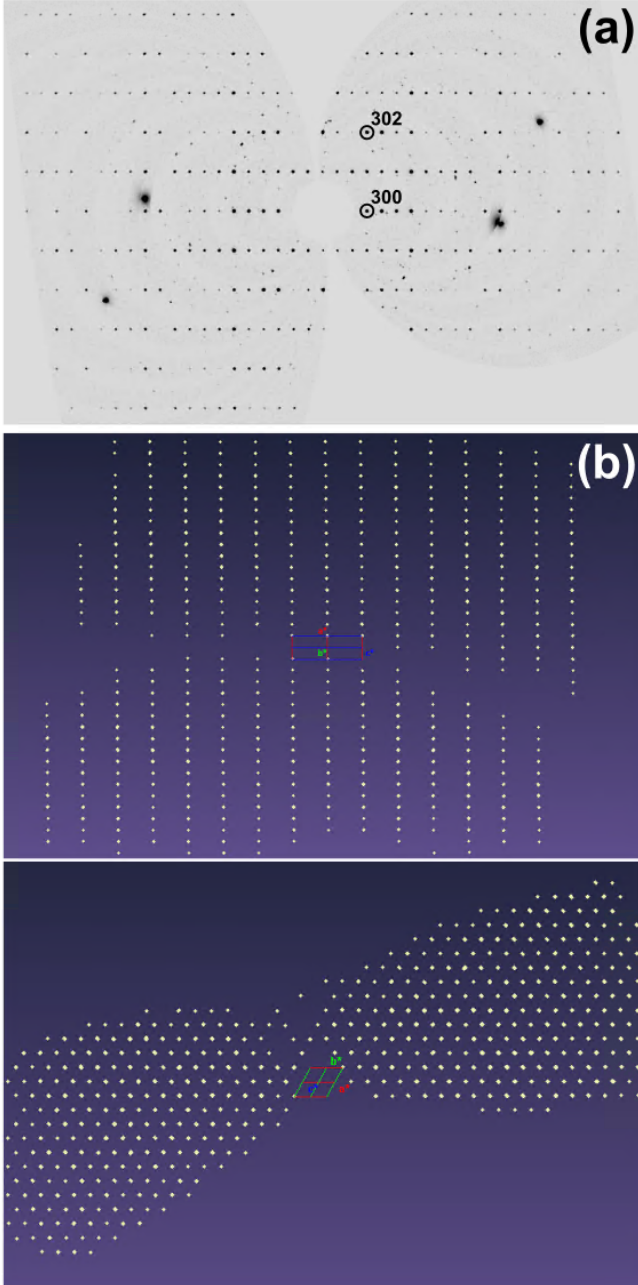
	Single Crystal	DFT
Crystal data		
Crystal system	Hexagonal	Hexagonal
Space group	$P6/m$	$P6/m$
Chemical formula	Ba[C_2O_5]	Ba[C_2O_5]
s.o.f (Ba4/Ba5)	0.90(1)/0.10(1)	0.90/0.10
M_r	241.4	
a (Å)	14.9484(7)	14.856
b (Å)	14.9484(7)	14.856
c (Å)	4.8464(2)	4.8310
α (°)	90.0	90.0
β (°)	90.0	90.0
γ (°)	120.0	120.0
V (Å^3)	937.86(7)	923.36
Z	12	12
Data collection		-
F_{000}	1296	-
θ range (°)	1.70–18.08	-
measured reflections	4537	-
independent reflections	1949	-
reflections $I > 2\sigma(I)$	1463	-
R_{int}	0.026	-
		-
Refinement		-
$R[F > 2\sigma(F)]$, $wR(F)$	0.034, 0.036	-
No. of reflections	1463	-
No. of parameters	94	-
No. of restraints	0	-
No. of constraints	2	-
$\Delta\rho_{max}$, $\Delta\rho_{min}$ (e Å^{-3})	1.47, -1.79	-

We observed a barium disorder in channels running along the *c*-axis. Fig. S 4 a shows a $y - z$ Fourier map (F_{obs}) for $x = 0$ along the channel. Two barium positions (0,0,0 and 0,0,0.5) could be identified, but the electron density on the 0,0,0 position is much smaller than on the 0,0,0.5 position. We refined the site occupation factor for the 0,0,0 and 0,0,0.5 barium atoms. An independent refinement results in one position at 0,0,0.5 with a high $s.o.f = 0.87(1)$ and one at 0,0,0 with a with low $s.o.f = 0.08(1)$. Within the experimental uncertainties the total occupation is $\approx 100\%$. Hence, we introduced a corresponding constraint for the total occupancy of the Ba atoms in the channel, resulting in $s.o.f = 0.90(1)$ for the 0,0,0.5 position and $s.o.f = 0.10(1)$ for the 0,0,0 position.

The weaker 0,0,0 Ba position becomes more pronounced in the difference Fourier map ($F_{obs} - F_{calc}$) after adding first only a barium atom on the 0,0,0.5 position (Fig. S 4 b). With respect to the difference Fourier map it seems possible that other Ba positions with a very small site occupation factor may be present in the channel along the [001] direction but had not been resolved from our diffraction data (Fig. S 4 c). Adding further Ba atoms in the channel does not result in a significantly reduced residual electron density ($\Delta\rho$) or an improved R-value. For the DFT calculations with VCA, we used site occupation factors of 0.90 and 0.10, respectively.
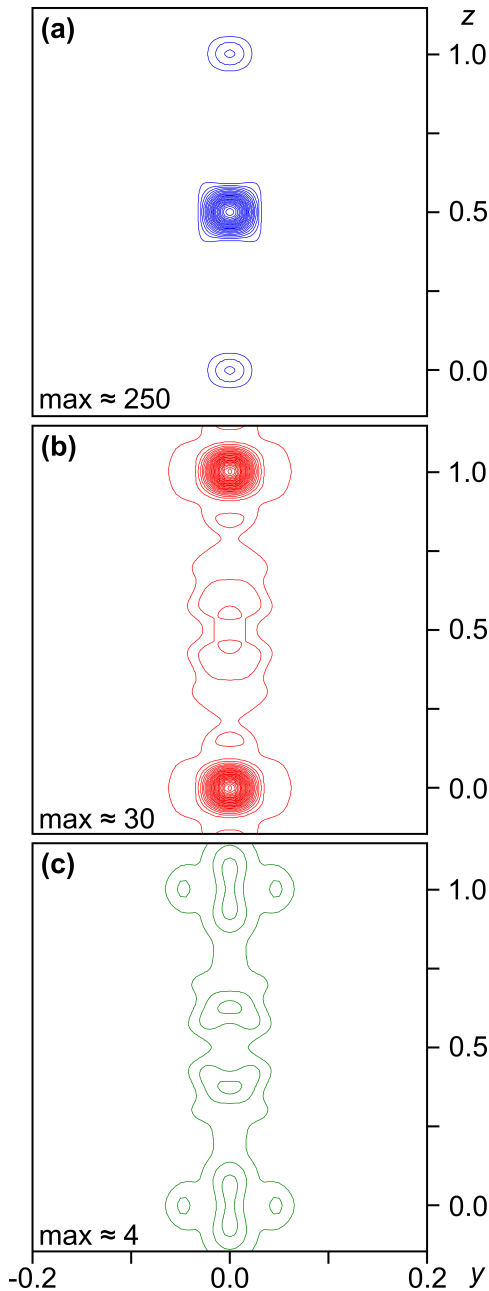
Figure S 5 shows the different coordination polyhedra of the Ba atoms with the surrounding oxygen atoms in $Ba[C_2O_5]$. The coordination numbers differ between 12 and 15. Ba1, Ba2 and Ba3 are in first approximation spherically coordinated while Ba4 and Ba5 are coordinated by a hexagonal prism of 12 oxygen atoms.
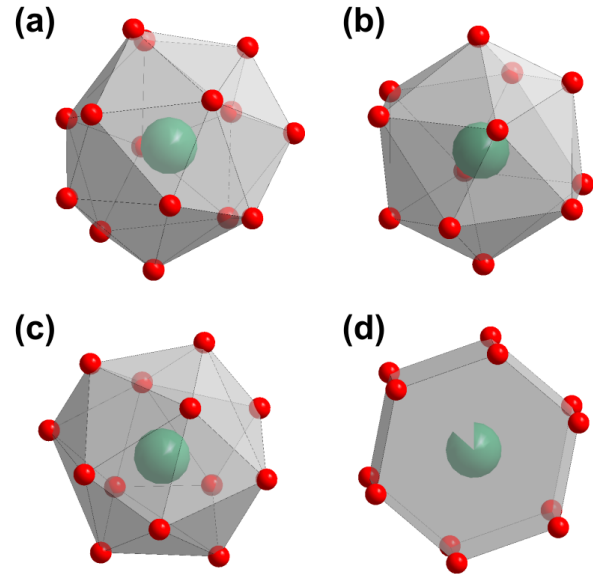

Figure S 5: Coordination polyhedra of different Ba atoms with surrounding oxygen atoms in $Ba[C_2O_5]$ with different coordination numbers (CN). (a) Ba1: CN = 15, (b) Ba2: CN = 12, (c) Ba3: CN = 13 and (d) Ba4/Ba5: CN = 12.

2.3. VCA calculations on $Ba[C_2O_5]$

The theoretical bulk modulus of $Ba[C_2O_5]$ between 5 GPa and 50 GPa was derived from DFT-based calculations using VCA. A 3rd-order Birch-Murnaghan equation of states (EOS) was fitted to unit cell volume obtained by the calculations between 5 GPa and 50 GPa using the software EOSFit7-GUI (Fig. S 6).[27–29]
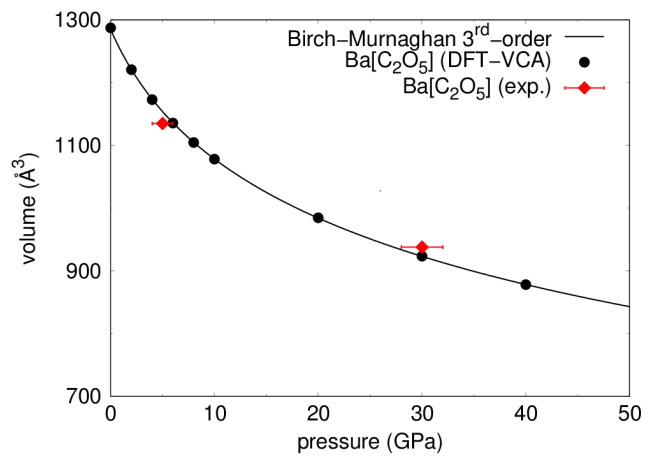
Figure S 6: Birch-Murnaghan EOS fitted to the unit cell volume of $Ba[C_2O_5]$ between 5 GPa and 50 GPa obtained by DFT-based calculations using VCA in comparison to the experimental data at 5(1) GPa and 30(2) GPa. Error-bars of the experimental unit cell volumes are smaller than the symbol-size.

Figure S 4: (a) Fourier map (F_{obs}) showing the two barium positions (0,0,0 and 0,0,0.5) along the [001] direction for $x = 0$. (b) Difference Fourier map ($F_{obs} - F_{calc}$) after adding a Ba atom at the 0,0,0.5 position, but not at 0,0,0 position. (c) Difference Fourier map after adding Ba atoms with partial occupancies on 0,0,0.5 and 0,0,0. The maximum of each map ($e^-/\text{Å}^3$) is shown.

The experimentally obtained unit cell volumes from the single crystal structure refinements at 5(1) GPa and 30(2) GPa are shown for comparison. The theoretical bulk modulus of $Ba[C_2O_5]$ is $K_0 = 36(1)$ GPa with $K_P = 5.8(1)$, which is consistent with the DFT data for $Pb[C_2O_5]$ ($K_0 = 36(3)$ GPa, $K_P = 5.9(3)$) and $Sr[C_2O_5]$ ($K_0 = 40(3)$ GPa, $K_P = 5.4(2)$) obtained in a similar pressure range.[4]
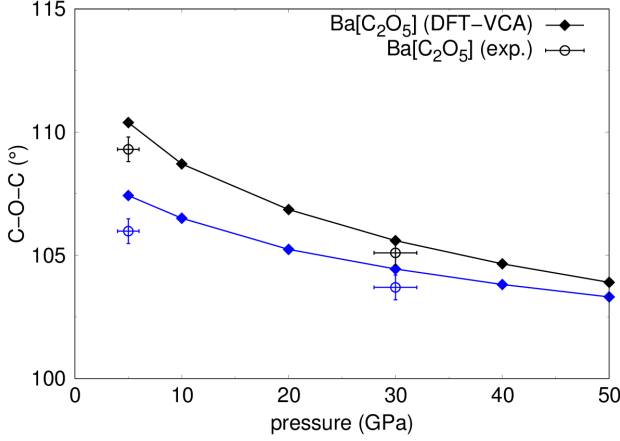

Figure S 7: C–O–C angle in the two symmetrically independent $[C_2O_5]^{2-}$-groups of $Ba[C_2O_5]$ between 5 GPa and 50 GPa from VCA calculations in comparison to experimental data at 5(1) GPa and 30(2) GPa.

We used the VCA calculations on $Ba[C_2O_5]$ to follow the evolution of the C–O–C angle in the pressure range between 5 GPa and 50 GPa. The C–O–C angle in both symmetrically independent $[C_2O_5]^{2-}$-groups increases slightly with decreasing pressure (Fig. S 7). This is in good agreement with the experimentally obtained data at 5(1) GPa and 30(2) GPa. Furthermore, the difference between the C–O–C angles in the $[C_2O_5]^{2-}$-groups increases at lower pressure.
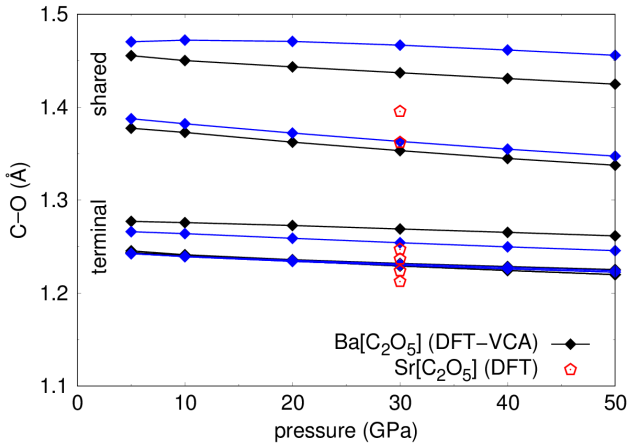

Figure S 8: C–O distance in the two symmetrically independent $[C_2O_5]^{2-}$-groups (black and blue lines) of $Ba[C_2O_5]$ between 5 GPa and 50 GPa from VCA calculations in comparison to DFT data of $Sr[C_2O_5]$ at 30 GPa.[30]

Figure S 8 shows the C–O distances in both $[C_2O_5]^{2-}$-groups of $Ba[C_2O_5]$. In contrast to the C–O–C angle, they remain approximately constant between 5 GPa and 50 GPa. The C–O distances to the terminal oxygen atoms

are significantly smaller than to the shared ones and in good agreement with the DFT data of $Sr[C_2O_5]$ at 30 GPa. In $Ba[C_2O_5]$ two noticeably different C–O distances to the shared oxygen atoms can be observed in agreement with the experimental data, while in $Sr[C_2O_5]$ their difference is very small.

2.4. Single crystal synchrotron X-ray diffraction at 5 GPa

We used the hexagonal structural model of $Ba[C_2O_5]$ determined at 30(2) GPa as a starting model to refine single crystal X-ray diffraction data obtained at 5(1) GPa. Table S 2 lists the experimental data refined in space group $P6/m$.

Table S 2: Structural parameters of disordered $Ba[C_2O_5]$ at 5(1) GPa from single crystal structure solution (ambient temperature) in hexagonal space group $P6/m$ in comparison to theoretical data derived from DFT calculations (athermal limit) on $Ba[C_2O_5]$ using VCA.

	Single Crystal	DFT
Crystal data		
Crystal system	Hexagonal	Hexagonal
Space group	$P6/m$	$P6/m$
Chemical formula	$Ba[C_2O_5]$	$Ba[C_2O_5]$
$s.o.f$ (Ba4/Ba5)	0.88(2)/0.12(2)	0.90/0.10
M_r	241.4	241.35
a (Å)	15.917(5)	15.832
b (Å)	15.917(5)	15.832
c (Å)	5.172(2)	5.3141
α (°)	90.0	90.0
β (°)	90.0	90.0
γ (°)	120.0	120.0
V (Å^3)	1134.8(7)	1153.52
Z	12	12
Data collection		-
F_{000}	1296	-
θ range (°)	1.60–17.62	-
measured reflections	6015	-
independent reflections	2413	-
reflections $I > 2\sigma(I)$	1008	-
R_{int}	0.057	-
		-
Refinement		-
$R[F > 2\sigma(F)]$, $wR(F)$	0.114, 0.087	-
No. of reflections	1008	-
No. of parameters	54	-
No. of restraints	0	-
No. of constraints	2	-
$\Delta\rho_{max}$, $\Delta\rho_{min}$ (e Å^{-3})	3.69, -2.31	-

The reflection intensity was significantly lower at 5 GPa, in contrast to the diffraction data 30 GPa. The atomic parameters were refined analogously to described above, but the displacement parameters of the carbon and oxygen atoms were refined isotropically to reduce the number of free parameters, as access to the reciprocal space is limited by the DAC, which typically shadows more than 60% of the reflections. The total occupancy of the Ba

atoms in the channel was constraint to one. The resulting site occupation factors are similar to the refinement at 30(2) GPa (*s.o.f* = 0.88(2) and *s.o.f* = 0.12(2)). Hence, the obtained chemical composition is $Ba[C_2O_5]$ within the experimental uncertainties. Theoretical crystallographic data on $Ba[C_2O_5]$ from DFT calculations had been obtained using VCA with site occupation factors of 0.90 and 0.10, respectively. We observed no significant difference between the structural models at 5(1) GPa and 30(2) GPa except an increase in the lattice parameters and the unit cell volume with decreasing pressure. Therefore, we assume that there is no phase transition in this pressure range.

References

(1) Pan, Y.; Wu, M.; Su, Q. Synthesis of Eu^{3+}-doped calcium and strontium carbonate phosphors at room temperature. *Mater. Res. Bull.* **2003**, *38*, 1537–1544, DOI: 10.1016/S0025-5408(03)00174-0

(2) Boehler, R. New diamond cell for single–crystal X-ray diffraction. *Rev. Sci. Instrum.* **2006**, *77*, 115103–1–115103–3, DOI: 10.1029/JB091iB05p04673

(3) Mao, H. K.; Xu, J.; Bell, P. M. Calibration of the ruby pressure gauge to 800 kbar under quasi-hydrostatic conditions. *J. Geophys. Res.* **1986**, *91*, 4673–4676, DOI: 10.1029/JB091iB05p04673

(4) Spahr, D.; König, J.; Bayarjargal, L.; Luchitskaia, R.; Milman, V.; Perlov, A.; Liermann, H.-P.; Winkler, B.; Synthesis and Structure of $Pb[C_2O_5]$: An Inorganic Pyrocarbonate Salt. *Inorg. Chem.* **2022**, *61*, 9855–9859, DOI: 10.1021/acs.inorgchem.2c01507

(5) Scelta, D.; Ceppatelli, M.; Ballerini, R.; Hajeb, A.; Peruzzini, M.; Bini, R. Sprayloading: A cryogenic deposition method for diamond anvil cell. *Rev. Sci. Instrum.* **2018**, *89*, 053903, DOI: 10.1063/1.5011286

(6) Bayarjargal, L.; Fruhner, C.-J.; Schrodt, N.; Winkler, B. $CaCO_3$ phase diagram studied with Raman spectroscopy at pressures up to 50 GPa and high temperatures and DFT modeling. *Phys. Earth Planet. Inter.* **2018**, *281*, 31–45, DOI: 10.1016/j.pepi.2018.05.002

(7) Wojdyr, M. *Fityk*: a general-purpose peak fitting program. *J. Appl. Cryst.* **2010**, *43*, 1126–1128, DOI: 10.1107/S0021889810030499

(8) Benedetti, L. R.; Loubeyre, P. Temperature gradients, wavelength-dependent emissivity, and accuracy of high and very-high temperatures measured in the laser-heated diamond cell. *High Press. Res.* **2004**, *24*, 423–455, DOI: 10.1080/08957950412331331718

(9) Du, Z.; Amulele, G.; Benedetti, L. R.; Lee, K. K. M. Mapping temperatures and temperature gradients during flash heating in a diamond-anvil cell. *Rev. Sci. Instrum.* **2013**, *84*, 075111, DOI: 10.1063/1.4813704

(10) Liermann, H.-P.; Konôpková, Z.; Morgenroth, W.; Glazyrin, K.; Bednarčik, J.; McBride, E. E.; Petitgirard, S.; Delitz, J. T.; Wendt, M.; Bican, Y.; Ehnes, A.; Schwark, I.; Rothkirch, A.; Tischer, M.; Heuer, J.; Schulte-Schrepping, H.; Kracht, T.; Franz, H. The Extreme Conditions Beamline P02.2 and the Extreme Conditions Science Infrastructure at PETRAIII. *J. Synchrotron Radiat.* **2014**, *22*, 908–924, DOI: 10.1107/S1600577515005937

(11) Prescher, C.; Prakapenka, V. B. *DIOPTAS*: a program for reduction of two-dimensional X-ray diffraction data and data exploration. *High. Press. Res.* **2015**, *35*, 223–230, DOI: 10.1080/08957959.2015.1059835

(12) Agilent, CrysAlis PRO, Yarnton, England, **2014**

(13) Petricek, V.; Dusek, M.; Palatinus, L. Crystallographic Computing System JANA2006: General features. *Z. Kristallogr.* **2014**, *229*, 345–352, DOI: 10.1515/zkri-2014-1737

(14) Sheldrick, G. M. *SHELXT* — Integrated space-group and crystal-structure determination. *Acta. Cryst.* **2015**, *A71*, 3–8, DOI: 10.1107/S2053273314026370

(15) Hohenberg, P.; Kohn, W. Inhomogeneous Electron Gas. *Phys. Rev.* **1967**, *136*, B864–B871, DOI: 10.1103/PhysRev.136.B864

(16) Perdew, J. P.; Burke, K.; Ernzerhof, M. Generalized Gradient Approximation Made Simple. *Phys. Rev. Lett.* **1996**, *77*, 3865–3868, DOI: 10.1103/PhysRevLett.77.3865

(17) Clark, S. J.; Segall, M. D.; Pickard, C. J.; Hasnip, P. J.; Probert, M. I. J.; Refson, K.; Payne, M. C. First principles methods using CASTEP. *Z. Kristallogr.* **2005**, *220*, 567–570, DOI: 10.1524/zkri.220.5.567.65075

(18) Lejaeghere, K.; Bihlmayer, G.; Björkman, T.; Blaha, P.; Blügel, S.; Blum, V.; Caliste, D.; Castelli, I. E.; Clark, S. J.; Dal Corso, A. et al. Reproducibility in density functional theory calculations of solids. *Science* **2016**, *351*, aad3000, DOI: 10.1126/science.aad3000

(19) Monkhorst, H. J.; Pack, J. D. Special points for Brillouin-zone integrations. *Phys. Rev. B* **1976**, *13*, 5188–5192, DOI: 10.1103/PhysRevB.13.5188

(20) Baroni, S.; de Gironcoli, S.; Dal Corso, A.; Giannozzi, P. Phonons and related crystal properties from density-functional perturbation theory. *Rev. Mod. Phys.* **2001**, *73*, 515–562, DOI: 10.1103/RevModPhys.73.515

(21) Refson, K.; Tulip, P. R.; Clark, S. J. Variational density-functional perturbation theory for dielectrics and lattice dynamics. *Phys. Rev. B* **2006**, *73*, 155114, DOI: 10.1103/PhysRevB.73.155114

(22) Miwa, K. Prediction of Raman spectra with ultrasoft pseudopotentials. *Phys. Rev. B* **2011**, *84*, 094304, DOI: 10.1103/PhysRevB.84.094304

(23) Winkler, B.; Pickard, C.; Milman, V. Applicability of a quantum mechanical 'virtual crystal approximation' to study Al/Si-disorder. *Chem. Phys. Lett.* **2002**, *362*, 266–270, DOI: 10.1016/S0009-2614(02)01029-1

(24) Datchi, F.; Mallick, B.; Salamat, A.; Ninet, S. Structure of Polymeric Carbon Dioxide CO_2-V. *Phys. Rev. Lett.* **2012**, *108*, 125701, DOI: 10.1103/PhysRevLett.108.125701

(25) Yoo, C.-S.; Iota, V.; Cynn, H. Nonlinear Carbon Dioxide at High Pressures and Temperatures. *Phys. Rev. Lett.* **2001**, *86*, 444–447, DOI: 10.1103/PhysRevLett.86.444

(26) Spek, A. L. Single-crystal structure validation with the program *PLATON*. *J. Appl. Cryst.* **2003**, *36*, 7–13, DOI: 10.1107/S0021889802022112

(27) Murnaghan, F. The Compressibility of Media under Extreme Pressures. *Proc. Natl. Acad. Sci.* **1944**, *30*, 244–247, DOI: 10.1073/pnas.30.9.244

(28) Birch, F. Finite Elastic Strain of Cubic Crystals. *Phys. Rev.* **1947**, *71*, 809–824, DOI: 10.1103/PhysRev.71.809

(29) Gonzalez-Platas, J.; Alvaro, M.; Nestola, F.; Angel, R. *EosFit7-GUI*: a new graphical user interface for equation of state calculations, analyses and teaching. *J. Appl. Cryst.* **2016**, *49*, 1377–1382, DOI: 10.1107/S1600576716008050

(30) Spahr, D.; König, J.; Bayarjargal, L.; Milman, V.; Perlov, A.; Liermann, H.-P.; Winkler, B. $Sr[C_2O_5]$ is an Inorganic Pyrocarbonate Salt with $[C_2O_5]^{2-}$ Complex Anions. *J. Am. Chem. Soc.* **2022**, *144*, 2899-2904, DOI: 10.1021/jacs.2c00351